Proceedings of the Canadian Society for Mechanical Engineering International Congress 2021
CSME Congress 2021
June 27-30, 2021, Charlottetown, PE, Canada

Realistic Representative Volume Element Generation for Sintered Solids Part 1: Algorithm for Volume Computation and Geometry Creation

D. Frank Thomas*, A .Y. Elruby, Sam Nakhla
Faculty of Engineering and Applied Science (Mechanical)
Memorial University of Newfoundland
*dft135@mun.ca

Abstract—The following work presents an algorithm for the generation of geometric models which function as realistic and accurate portrayals of powder-based porous sintered solids in both form and function. The code base was developed in Python for use in ABAQUS finite element software. The development of key modules such as the smart compaction, particle settling, and rapid volume computation processes are described in detail. Geometric models were evaluated for accuracy, computational efficiency, and physical characteristics at various porosities. Part 2 of this work investigates the finite element analysis results of these models compared to experimental data.

Keywords: microstructure modelling, porous sintered solid, finite element analysis, representative volume element

I. INTRODUCTION

The presence of voids is known to have a significant effect on mechanical behavior [1]. Though these voids are generally thought of as defects to be minimized, applications with a very limited range of viable materials stand to benefit from the ability to tailor a material's mechanical properties by inducing uniformly distributed voids, i.e. inducing porosity in the micro- or meso-structure. Recent developments in the field of particle-based additive manufacturing have popularized near-net shape fabrication methods whose structure closely resembles that of sintered compacts from powder metallurgy [2] [3] [4].The voids observed in sintered materials are characteristically distinct from the voids observed in traditional materials, having segmented and bulging surfaces rather than continuous ellipsoidal shapes [5]. Minimal research has been conducted specifically to investigate the effect of porosity on the mechanical behavior of sintered materials, and the abnormal characteristics of void defects in powder-based materials eliminate the type of uniform void models used to simulate the behavior of traditional porous materials [6]. The algorithm presented in this work produces realistic powder-based microstructure models of a specific porosity from randomly placed particles using novel compaction and rapid volume computation processes.

II. ALGORITHM

A. Inputs & Population

The realistic model generation algorithm requires two fundamental pieces of information: the target porosity of the final specimen and a description of the particles to be used. The porosity term denotes the fractional volumetric porosity of the representative volume element as seen in (1). In this expression, V_T represents the volume enclosed by the RVE and V_M is the total volume of the intersecting geometric entities.

$$P = \frac{1}{V_T}(V_T - V_M) \tag{1}$$

A description of the base particles may be provided in the form of an upper and lower bound on particle diameter, a normal distribution, or alternatively as a probability or cumulative distribution function. The population algorithm produces a set of randomly placed non-intersecting particles whose centers reside within a bounding box of a specified side length L. Particle coordinates and diameters are randomly generated in accordance with the particle size description. Once generated, a prospective particle is evaluated against all previously placed particles to detect particle-particle intersection; if none are detected the particle characteristics are appended to the set, otherwise the particle is rejected. This process loops until the number of consecutive rejections exceeds some specified limit. The final particle configuration is returned and passed to the compaction module.

B. Smart Compaction Algorithm

Given three known values (boundary length, particle volume, and target porosity) the compaction module will begin to alter particle positions, drawing each particle center proportionally toward the RVE center until the void fraction is determined to be within an acceptable margin of the target porosity. This numerical root finding method uses linear extrapolation to suggest compaction levels such that the RVE porosity approaches the target porosity with precision and efficiency. The rapid root-finding algorithm first queries the total volume

(V_o) of particles enclosed by the bounding box by passing the newly populated particle configuration to the volume computation module. An initial compaction multiplier of 5% is applied to the coordinates of each particle, drawing them uniformly toward the origin – see (2).

$$[X_1\ Y_1\ Z_1] = c_1[X_0\ Y_0\ Z_0] \quad (2)$$

Where $c_1 = (1 - 0.05)$ is the first attempted compaction multiplier. Since the populated configuration is not compacted whatsoever the initial compaction is $c_0 = 1$. The volume of the compacted configuration is evaluated and returns V_1. Porosities p_0 and p_1 are calculated from V_0 and V_1 respectively per equation 1. A new compaction multiplier is predicted from these two data points as seen below.

$$c_{i+1} = c_i + (c_{i-1} - c_i)\left(\frac{P - p_i}{p_{i-1} - p_i}\right) \quad (3)$$

The first computed compaction multiplier is then applied to the initial particle configuration per (2). Unlike the previous iteration, the new particle coordinates are individually re-arranged to emulate the natural settling behavior of free particles. The volume of the settled configuration is computed and used to determine the next porosity p_2. This process of compaction, settling, volume computation, and comparison is repeated until the achieved porosity falls within an acceptable margin of the target porosity.

C. Particle Arrangement

The particle arrangement function evaluates each individual particle, compiling information about each of the surrounding

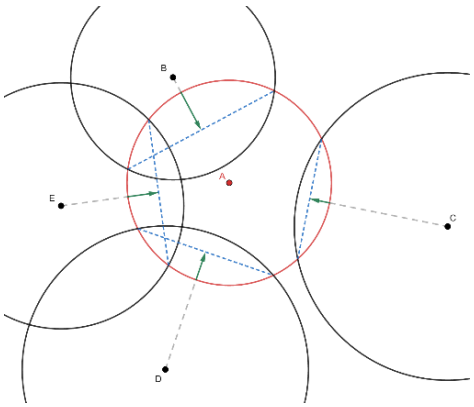

Figure 1. Particles Pre-Arrangement

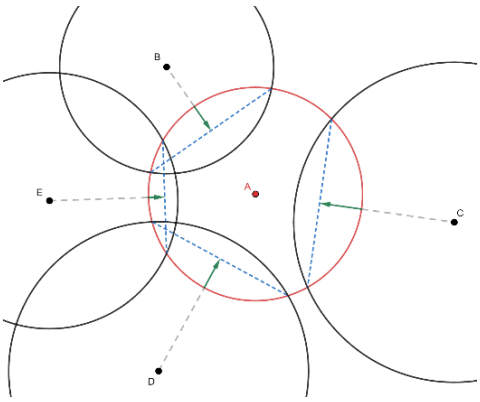

Figure 2. Arranged (Settled) Particles

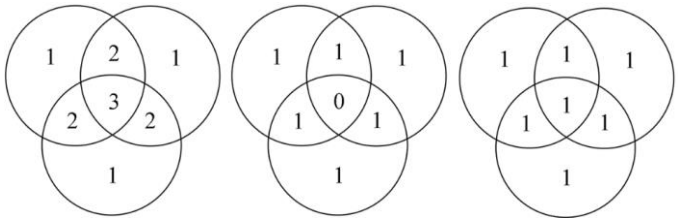

Figure 3. Inclusion-Exclusion Principle

intersecting particles. A separation vector V_{AB} is calculated from the coordinates and radii of two overlapping particles A and B such that translation of particle A by V_{AB} separates the particles from each other. In the case of A being intersected by two or more particles, a single relocation vector is constructed from the individual separation vectors.

$$R_A = V_{AB} + V_{AC} + V_{AD} \cdots \quad (4)$$

The new coordinates of particle A are updated prior to evaluating the next particle for rearrangement. The resulting configuration presents a more realistic model of particle compaction than scalar multiplication alone.

III. Rapid Volume Computation

A. Principle

The volume computation module evaluates the volume of intersecting hard spheres algebraically by decomposing particles into regions of n^{th} degree overlap. These regions are then tallied according to the inclusion-exclusion principle such that the volume of every region is counted once. In general, the total volume of any union of intersecting hard spheres is found by subtracting the sum of the volume of even-degree overlap regions from the total volume of odd-degree overlap regions.

B. 2D Cases

1) Excluded Regions

A particle that is intersected by another particle in 2D will form two points of intersection that describe a line of intersection some normal distance D from the center of each particle. If the distance between the centers of each particle is $\overline{AB}$ then the distance from point A to the intersection line is

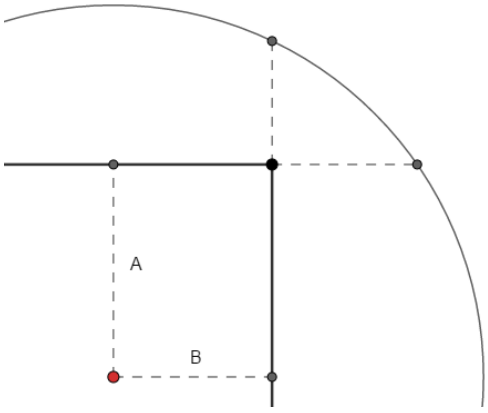

Figure 4. Two-Boundary Overlap

calculated per (5).

$$D_A = \frac{r_A^2 - r_B^2 + \overline{AB}^2}{2\overline{AB}} \quad (5)$$

The following relationship also applies:

$$D_B = \overline{AB} - D_A \quad (6)$$

The area exterior to the intersection line is now calculated per (7). This equation is also used to calculate the area of a particle exterior to a boundary, where the distance term is simply the normal distance from the particle center to the boundary line.

$$\boldsymbol{A_{A,B}} = r_A\left(r_A \operatorname{acos}\left(\frac{D_A}{r_A}\right) - D_A\sqrt{1-\left(\frac{D_A}{r_A}\right)^2}\right) \quad (7)$$

2) Included Regions

The 1st degree region of inclusion is of course equal to the area of a circle radius r_A. Regions of 3rd degree overlap include the portion of a particle exterior to two boundary lines, the portion of a particle-particle overlap exterior to one boundary, and any area common to three particles. In the first case the region exterior to a set of perpendicular boundary lines is found by decomposing the particle into familiar cases. The figure below features two 2nd degree regions at distances $\bar{A}$ and $\bar{B}$ from their respective boundaries. To find the area of the region common to both caps we combine one-half the sum of the area of these regions, add the area of the rectangle $A * B$ and subtract one-quarter the area of the circle.

$$\frac{r_A}{2}\left[r_A\left(\operatorname{acos}\frac{A}{r_A} + \operatorname{acos}\frac{B}{r_A}\right) - A^* - B^*\right] + AB - \frac{\pi r_A^2}{4} \quad (8)$$

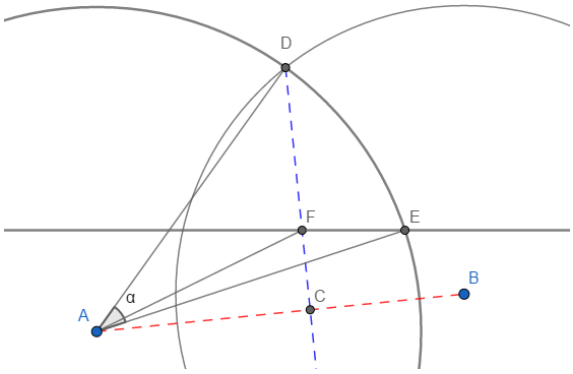

Figure 5. Two-Particle Overlap at Boundary

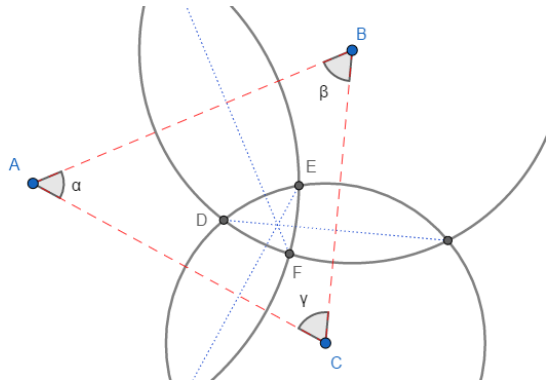

Figure 6. Three-Particle Overlap

Where $A^* = A\sqrt{1-\left(\frac{A}{r_A}\right)^2}$ and $B^* = B\sqrt{1-\left(\frac{A}{r_A}\right)^2}$.

The case of particle-particle intersection at a boundary requires the circular segment DAE from Figure 5 to be decomposed into triangular regions ADF and AEF to isolate the area of the circular wedge formed by line segments DF and EF. Given coordinates of points $A, D, E, \& F$ this is easily accomplished. We have chosen Heron's semiperimeter formulation to calculate the area of the triangles [7].

The case of three-particle overlap is calculated as follows:

$$T_{ABC} + \frac{1}{2}(A_{AB} + A_{AC} + A_{BC}) - \frac{1}{2}(\alpha r_A^2 + \beta r_B^2 + \gamma r_C^2) \quad (9)$$

Where T_{ABC} is the area of triangle ABC, A_{AB} is the area of the region common to particles A and B, and the angles α, β, γ are noted in Figure 6 [8].

C. 3D Cases

1) Spherical Cap

The 3D case follows the same principles as the 2D case with notably more unique region overlap configurations. The intersection of spheres A & B defines a circle situated on a plane of intersection with a unit normal in the direction of $\overrightarrow{AB}$. The normal distance from point A to this plane is calculated again using (5). The region of a sphere exterior to an intersecting plane is known as a spherical cap and the volume is calculated from (10).

$$V_{A,B} = \frac{\pi}{3}(r_A - D_A)^2(2r_A + D_A) \quad (10)$$

2) Spherical Wedge

When a sphere is intersected by two non-parallel planes whose line of intersection passes through the surface of the sphere, a 2nd order overlap region is formed. This region is common to both spherical caps and can be decomposed into two spherical wedges separated by the plane defined by the sphere center and the line of plane-plane intersection. Each of the resultant spherical wedges is described by a unique normal distance and wedge angle – see (11) [9].

$$V_{wA} = \frac{1}{3}r_A^3\left[\pi - 2\operatorname{asin}\left(\frac{r_A \sin\alpha}{\sqrt{r_A^2 - A^2}}\right)\right] \quad (11)$$

3) Spherical Tetrahedron

The 3rd degree overlap region of a sphere occurs when three intersecting planes meet at a point that lies within the sphere. The resultant shape resembles a tetrahedron with three straight lines, three curved lines, three flat faces and one curved face. The volume of the region is constructed from the regular tetrahedron described by the four aforementioned points, the volume of a spherical cap contained by a spherical triangle, and three wedges which compensate for the missing edge portions of the cap section.

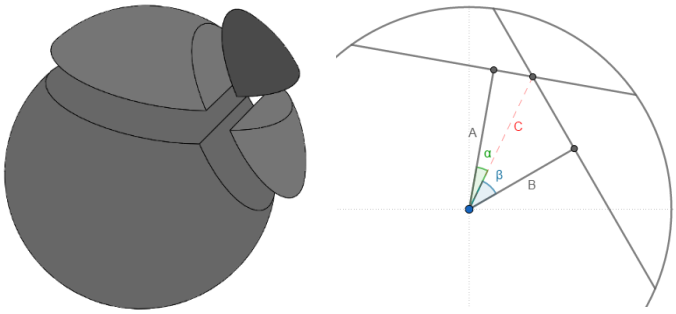

Figure 7. Spherical Wedge Deconstruction

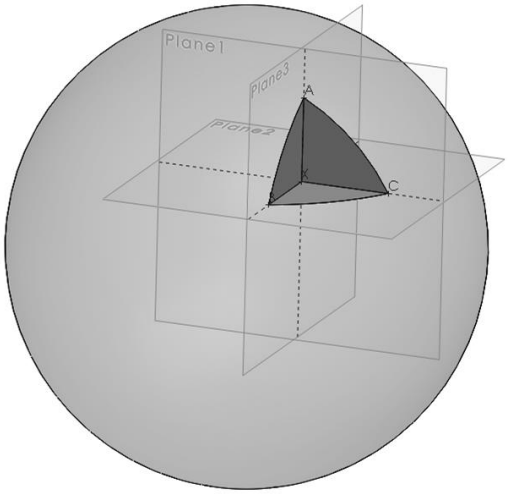

Figure 8. Isolation of Spherical Tetrahedron

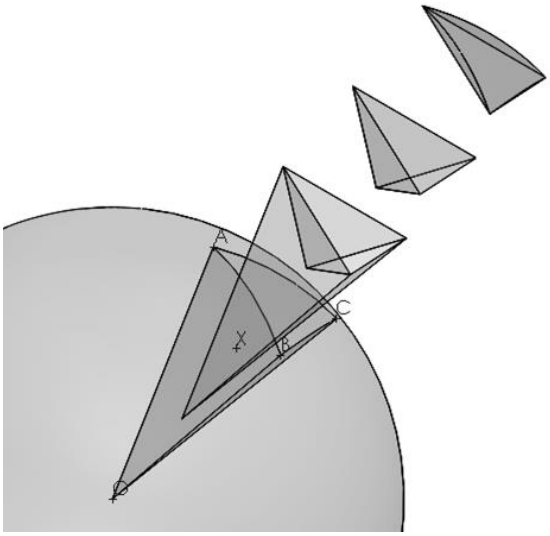

Figure 9. Decomposition of Spherical Tetrahedron

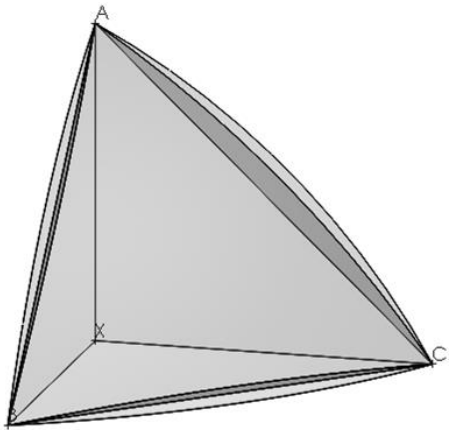

Figure 10. Spherical Wedge Correction

TABLE 1. GEOMETRIC MODEL ACCURACY

Porosity	**Measured Volume**		**% Difference**	
	2D	***3D***	***2D***	***3D***
20%	79.944%	79.979%	0.07%	0.03%
15%	84.977%	84.916%	0.03%	0.10%
10%	89.949%	89.987%	0.06%	0.01%
5%	94.922%	94.938%	0.08%	0.07%
4%	95.894%	95.941%	0.11%	0.06%
3%	96.974%	96.876%	0.03%	0.13%

IV. RESULTS

A. Accuracy & Efficiency

Table 1 shows the accuracy achieved by the model generation algorithm at various target porosities. Each model was generated as a CAD model and measured using onboard geometry tools. The measurements provided by the CAD software are the result of mesh-element volume computation. Each of the measured volumes is slightly less than the target volume, likely due to the entirely positive curvature of each models surface – a mesh element will neglect miniscule caps when approximating the volume of elements on a positively curved surface. Given the discretization error inherent in this measurement process and the low percent difference between the theoretical and measured volumes we conclude that both the rapid volume computation and particle compaction modules are functioning as intended.

Figures 11 and 12 demonstrate the efficacy of the smart compaction algorithm in 2D and 3D respectively. In both cases the target porosity was set to 5% with a margin of 10^{-12}. In both cases the algorithm appears to converge on the target porosity by iteration 5. The time elapsed during these computations was arbitrarily short. We observe that the compaction algorithm as a whole is highly effective, precise, and computationally efficient.

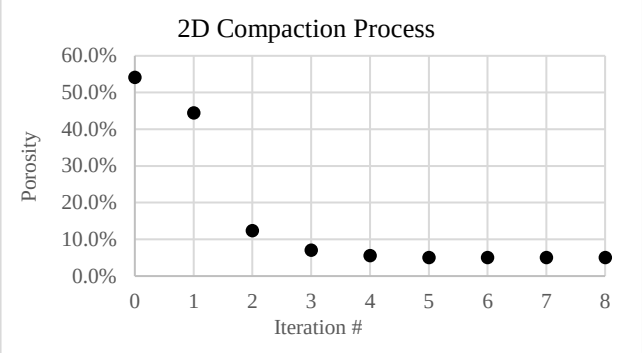

Figure 11. 2D Compaction Plot

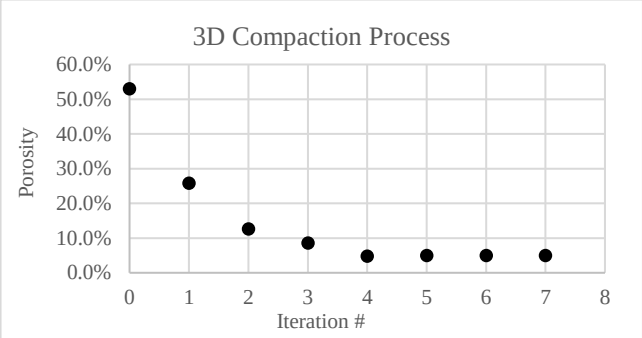

Figure 12. 3D Compaction Plot

B. Realistic Structure Generation

Figures 13 through 16 show the compaction process from population to final compaction in 2D and 3D. We observe that in both cases particles settle and compact in a seemingly natural manner. Voids appear uniformly distributed and no two particles appear to intersect disproportionately. The void characteristics in these specimens resemble those observed in sintered compact microstructures.

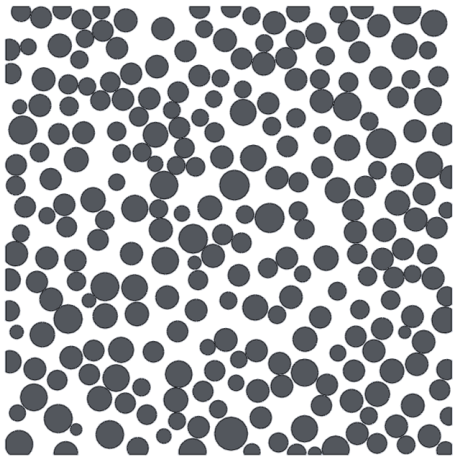

Figure 13. Initial Population - 2D

Figure 14. Sintered Particle Model - 2D

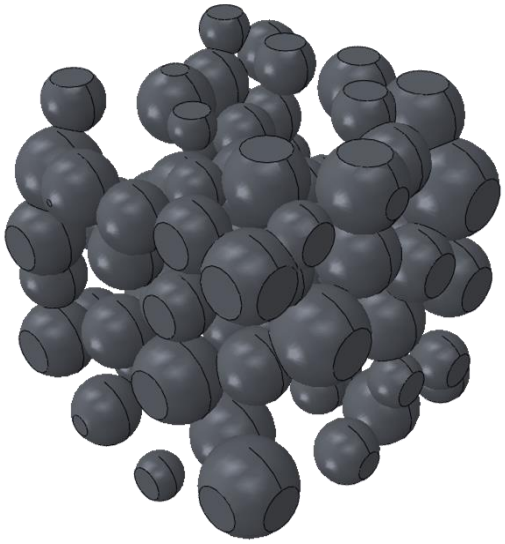

Figure 15. Initial Population - 3D

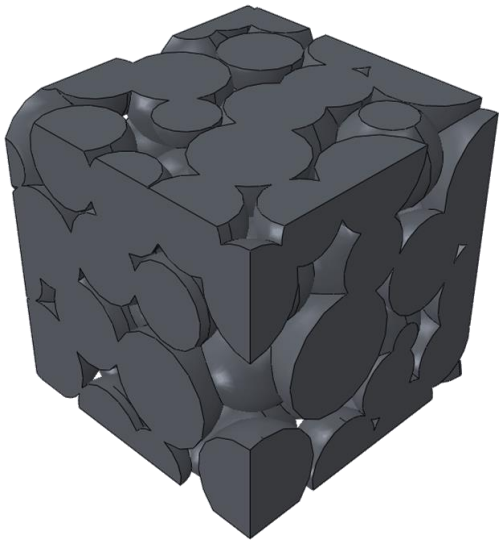

Figure 16. Sintered Particle Model - 3D

[1] H. H. Hausner, "The effect of porosity on the structure of sintered metals," *Journal of the Japan Society of Powder and Powder Metallurgy,* vol. 7, no. 2, pp. 58-72, 1960.

[2] G. D. Cremer, "Powder Metallurgy". United States of America Patent 2,355,954, 15 August 1944.

[3] J. Sedlak, D. Rican, M. Piska and L. Rozkosny, "Study of Materials Produced by Powder Metallurgy Using Classical and Modern Additive Laser Technology," in *25th DAAAM International Symposium on Intelligent Manufacturing and Automation*, Vienna, 2014.

[4] K. Yamaguchi, N. Takakura and S. Imatani, "Compaction and sintering characteristics of composite metal powders," *Journal of Materials Processing Technology,* vol. 63, no. 1-3, pp. 364-369, 1997.

[5] P. Fischer, H. Leber, V. Romano, H. P. Weber, N. P. Karapatis, C. André and R. Glardon, "Microstructure of near-infrared pulsed laser sintered titanium samples," *Applied Physics A,* vol. 78, no. 8, pp. 1219-1227, 2004.

[6] P. R. Woodmansee, "A finite element analysis of porosity effect on materials," 1989.

[7] W. Dunham, "Heron's Formula for Triangular Area," in *Journey through Genius: The Great Theorems of Mathematics*, New York, Wiley, 1990, pp. 113-132.

[8] M. P. Fewell, "Area of Common Overlap of Three Circles," Defence Science and Technology Division, Edinburgh, 2006.

[9] K. D. Gibson and H. A. Scheraga, "Exact calculation of the volume and surface area of fused hard-sphere molecules with unequal atomic radii," *Molecular Physics,* vol. 62, no. 5, pp. 1247-1265, 1987.